Astron. Astrophys. 276, 320–326 (1993)

ASTRONOMY AND ASTROPHYSICS

The ESO atmospheric temporal coherence monitor dedicated to high angular resolution imaging

Bruno Lopez[1] **and Marc Sarazin**[2]

[1] O.C.A Dpt. Fresnel - URA CNRS 1361 B.P. 229 - F-06304 Nice Cedex 4

[2] European Southern Observatory, Karl-Schwarzschild Str. 2, W-8046 Garching bei München, Germany

Received February 23, accepted April 9, 1993

Abstract. Seeing monitors using the differential image motion method were developed in the eighties for several site studies worldwide. Such an instrument has been included in the Astronomical Weather Station of La Silla, now part of standard astronomical observing in the observatory. In preparation for the interferometric mode of the VLT at Cerro Paranal, a new type of measurement has been undertaken to understand the physics of atmospheric motion and its relation to the temporal coherence of the wavefront at the telescope level. The concept of the coherence monitor is described and the first results of continuous monitoring with a prototype instrument are presented.

Key words: technics: interferometric – site testing – atmospheric effects

1. Introduction

The development of high resolution imaging techniques requires constant improvement of the operational tools. In particular, the performance of observations made by interferometry is extremely dependent on the quality of atmospheric seeing. A monitoring of the relevant atmospheric parameters is therefore essential.

The signal to noise ratio for long baseline interferometry (Roddier & Léna 1984) is related to the Fried parameter r_0 at least with a third power law and is proportional to the exposure time τ. The longest permissible or equivalently, the optimum exposure time which determines the depth of the recorded images, is limited by the degree of coherence of the turbulent atmosphere. That is to say the integration time has to be short enough to preserve the high spatial frequency content of the observed signal otherwise blurred by the wavefront corrugation.

While r_0 statistics are nowadays better understood, we still have a poor quantitative knowledge of the wavefront temporal coherence which was monitored only for a few nights over various sites (Scaddan & Walker 1978; Aime et al. 1986; Vernin et al. 1991). It is an independent random parameter without any systematic correlation with the Fried quantity. Due to its large expected variance, the optimum exposure time has a significant weight in the instantaneous signal to noise ratio in spite of its weak power dependency.

Whatever the way to observe (Adaptive Optics, Long Baseline Interferometry or Speckle Interferometry), the optimum exposure time is related to the horizontal motion of the turbulent atmosphere (Sect. 2.2). The Differential Image Motion Method (DIMM) summarized in Sect. 3 has proven its efficiency for the monitoring of r_0 (Fried 1975; Sarazin & Roddier 1990). A method based on the temporal correlation of image motion had been previously proposed for the qualitative study of τ (Müller et al. 1988; Abitbol et al. 1991). Here, this paper presents another simple and promising method recently tested at ESO observatories to obtain quantitative estimates of this parameter.

The DIMM principle is again used but a new theory based on the analysis of the velocity of image motion instead of temporal correlation leads to the statistical measure of the velocity of the turbulent layers as shown in Sect. 4. The ESO seeing monitors have been adapted to this purpose. The necessary instrumental modifications consist in the use of a scanning mirror which increases the individual image acquisition rate up to 500 Hz (Sect. 4.2). First results of monitoring made at La Silla are presented in Sect. 5.

Scientifically, a better understanding of site behavior for high resolution imaging will be achieved. Moreover the parallel monitoring of τ will improve the strategy of observation in interferometry, permitting to adapt astronomical programs, in particular for faint sources, to the chaotic nature of the Earth's atmosphere.

Send offprint requests to: Bruno Lopez

2. Physics of the wavefront temporal characteristics

2.1. Mechanism of turbulence induction, Fried parameter

Under typical astronomical conditions, the random spatial variations of the index of refraction of air depends mainly on temperature fluctuations through the Earth's atmosphere. The effect of water vapor and pressure variations is generally small enough to be ignored. Because of the low kinematic viscosity of air, the Reynolds number of the atmosphere in motion always exceeds its critical value which allows for well developed mechanical turbulence. The mixing between warm and cold air masses therefore creates inhomogeneities of the temperature field, responsible for the phase perturbations detected on a wavefront propagating through it.

The Kolmogorov model which applies for fluid turbulence is commonly used to describe, statistically, spatial structures of the atmosphere. It assumes that the kinetic energy, contained in a turbulent flow, is transferred without any loss from the largest eddies to the smallest ones, until being finally dissipated by viscosity. The phase shift φ of the corrugation is usually given in terms of structure functions :

$$D_\varphi(r) = <|\varphi(x) - \varphi(x-r)|^2> = 2.91\left(\frac{2\pi}{\lambda}\right)^2 \int_0^H C_n^2(h)\,dh\,r^{5/3} \quad (1)$$

where the scintillation phenomenon on the wavefront has been neglected under the assumption called the near field approximation. The subscript of D implies that the random variable is the received phase field. x and r are lengths in the horizontal plane. The 5/3 power law results from the Kolmogorov cascade, λ is the wavelength. The structure coefficient $C_n^2(h)$, which depends on altitude, relates to the amount of refractive index fluctuations affecting optical propagation. As the phase shift of the perturbations is caused by several regions of turbulence over the atmospheric column, the structure function at ground level is related to the integral of $C_n^2(h)$. This equation is valid in the inertial range, bounded by the inner scale of turbulence l_0, at which viscous dissipation arises, and by the outer scale L_0 or equivalently the size of the largest eddies maintaining isotropic properties.

One very convenient quantity, outlined by Fried, is the critical pupil diameter r_0 under which the resolving power of a telescope is diffraction limited. Above this value, seeing effects linked to the turbulent atmosphere seriously affect image quality. The Fried parameter r_0 is equally defined as the diameter of the mean area of optical coherence on the wavefront, within which the mean square phase variations are less than 1 rd^2:

$$r_0 = \left[0.423\left(\frac{2\pi}{\lambda}\right)\int C_n^2(h)dh\right]^{-3/5} \quad (2)$$

2.2. Wavefront temporal characteristics

In astronomy, high resolution imagery implies both a high signal level in the recorded image and short enough exposures for a correct signal sampling. A major constraint is therefore imposed by the time variations of wavefront perturbations (or coherence time for the atmosphere). The coherence length r_0, as given by Fried, is a statistical parameter which does not invoke any temporal change. In a simplified model, the temporal change is attributed to the horizontal motion of a frozen atmosphere, acting as a single moving phase screen. The shift of equally frozen phase corrugation moves therefore at the mean wind velocity and in the mean wind direction. This assumption named the Taylor hypothesis allows to define the coherence time of the kinematic atmosphere using the simple equation,

$$\tau = \frac{r_0}{v} \quad (3)$$

where τ is clearly the time required to pass over an area of coherence r_0.

In fact, to be consistent with reality, several moving turbulent layers must be considered. In particular, the case of speckle interferometry illustrates the inadequacy of the Taylor model: considering ad absurdum a telescope of infinite diameter, the speckle pattern observed would not be affected by the motion of a single frozen atmospheric layer. It is the dispersion velocity among different layers which induces a phase corrugation change on the wavefront, and consequently onto the speckle pattern. The multiple atmospheric layers model illustrated in Fig. 1 provides a more realistic picture in which the motion of

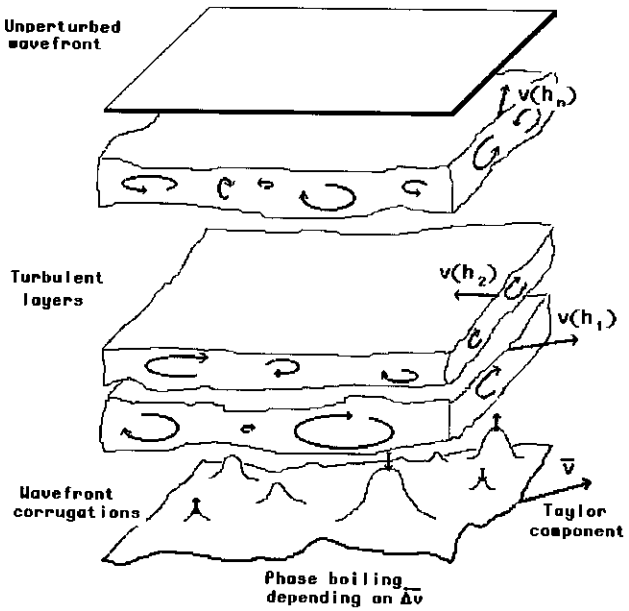

Fig. 1. The kinematic model of multiple and thin atmospheric layers moving independently of one another

Table 1. Main temporal coherence parameter of high resolution imaging modes.

Observing mode	Atmospheric parameter
Speckle Interferometry	$r_0 / \Delta v$
Adaptive Optics	r_0 / v^*
Michelson Interferometry	r_0 / v^*

speckles is characterized by the speckle life time (or speckle boiling time) following Roddier et al. 1982:

$$\tau = \frac{r_0}{\overline{\Delta v}} \tag{4}$$

with $\overline{\Delta v}$, the average dispersion velocity, given by:

$$\overline{\Delta v} = \left[\frac{\int_0^\infty |\, v(h)\,|^2\, C_n^2(h) dh}{\int_0^\infty C_n^2\,(h)\, dh} - \left| \frac{\int_0^\infty v(h) C_n^2(h)\, dh}{\int_0^\infty C_n^2\,(h) dh} \right|^2 \right]^{1/2} \tag{5}$$

where $v(h)$ is the wind velocity at altitude h.

For the Michelson interferometry case, to which the adaptive optic technique and the long baseline interferometry belong, the relation between the turbulent atmosphere and the optimum response time or exposure time for fringe pattern is again different. The transit time of perturbations over the telescope pupil determines the coherence time τ for Milchelson interferometry:

$$\tau = \frac{r_0}{v^*} \tag{6}$$

which now depends on a mean characteristic velocity of the turbulent layers v^* defined as:

$$v^* = \left[\frac{\int_0^\infty |\, v(h)\,|^{5/3}\, C_n^2(h)\, dh}{\int_0^\infty C_n^2(h)\, dh} \right]^{3/5} \tag{7}$$

Michelson interferometry is in fact a complex field which should be subdivided into specific modes in order to obtain more accurate relationships. One of them is long baseline interferometry where the outer scale of turbulence has some influence on the lifetime of the interference fringes.

Consequently, for a model of atmosphere constituted by multiple turbulent layers, each observing mode has its own requirement summarized in Table 1, being either the longest permissible exposure time or, as for adaptive optics, the response time which is best adapted to the evolution of wavefront corrugation.

3. Description of the differential motion monitor

3.1. Classical differential image motion monitor operation

The presence of turbulence in the Earth's atmosphere causes the stellar image formed by a telescope of small diameter to move randomly. The position of the stellar image in the focal plane is directly related to the tilt angle of the wavefront with regard to the entrance pupil plane of the telescope. According to theoretical calculations, the atmospheric turbulence can be estimated through the variance of the image motion. In practice, in order to measure accurately a rough mean square angle of arrival of the order of 0.1 arcsec^2 it is necessary to avoid any side-effect due to tracking errors of the telescope. For this purpose, Fried (1975) suggested to use the differential motion method where two separated apertures are used to form two different images of the same star. The differential motion of these images is then analyzed instead of their absolute motion. The formalism of the theory has been analytically described by Roddier (1981). Two structure functions for the angle of arrival of light α are derived in the directions parallel and perpendicular to the subpupil separation:

$$D_{\alpha,\parallel} = 2\lambda^2\, r_0^{-5/3}(0.179\, D^{-1/3} - 0.0968\, d^{-1/3}) \tag{8}$$

$$D_{\alpha,\perp} = 2\lambda^2\, r_0^{-5/3}(0.179\, D^{-1/3} - 0.145\, d^{-1/3}) \tag{9}$$

where D is the subpupils diameter and d their separation center to center.

Assuming that the turbulence characteristics is stationary, the structure functions are determined through a set of measures of wavefront slope differences. The Fried parameter r_0 is then deduced from the above relations.

3.2. DIMM system description

The differential image motion method has been extensively used at ESO to predict the quality of the image an astronomical large telescope would produce. Long term surveys of seeing conditions were performed, particularly for the search for the observatory site for the European Very Large Telescope.

The theory of differential motion is reviewed in Sarazin & Roddier (1990), along with a description of the seeing monitor instruments in use since 1987. The seeing monitors are Cassegrain telescopes of 35 cm diameter. The entrance pupil is re-imaged behind the Cassegrain focus by means of a Fabry lens. To obtain dual star images, whose relative motion in the image plane represent local wavefront tilt differences, a pupil mask associated with a roof prism is installed in the conjugate of the entrance pupil plane taken at the primary mirror level. The subpupils are realized by two holes in the pupil mask. As the prism splits the two beams, two separate images of the star are further formed in the image plane. The detector used is a microchannel plate image inverter intensifier tube on a 576x384 frame transfer CCD. Each stellar image covers an area of at least 3x3 pixels with a pixel angular size of 0.88 arcsec. The uncertainty in the determination of the relative positions of the image centroids corresponds to a noise of variance N_α^2:

$$N_\alpha^2 = 0.01 \pm 0.002\ \text{pixel}^2 \tag{10}$$

as measured in the laboratory for circular images. An electromagnetic shutter is used to obtain 10 ms exposure time per frame which is most of the time short enough to freeze the turbulence effects. Data reduction is made in real time after 200 differential image positions are sampled and leads to one r_0 estimate every 2 minutes.

4. Description of the coherence monitor

4.1. Velocity of differential motion

The differential image motion principle is a practical means for an experimental diagnosis of the temporal dependence of the

atmospheric effects on either speckle interferometry or Michelson interferometry. Indeed, the analysis of the velocity of the wavefront slope or, in other words, of the differential image motion velocity at the focus of a small telescope, contains the necessary statistical information on the velocity of the turbulent layers (Lopez & Sarazin 1991). The optimum exposure times, defined in Sect. 2, which are linked to the vertical distribution of wind and turbulence in the atmosphere can then be derived.

The new method consists of extending the differential image motion theory to a kinematic model for the atmosphere. The study of the tilt velocity rather than of the tilt amplitude only leads then to the following structure function along any direction of the pupil plane making an angle γ with the subpupil separation axis (Lopez 1992):

$$D_{\frac{\partial\alpha}{\partial t},\gamma} = 2 \cdot 0.128\lambda^2 r_0^{-5/3} D^{-7/3} \cdot \left(\overline{v}^2(1+2\cos^2(\theta-\gamma)) + 2\overline{\Delta v}^2\right)\left(1 - f(\overline{v},\theta,\overline{\Delta v},D,d,\gamma)\right) \quad (11)$$

The quantities $\overline{v}$, θ and $\overline{\Delta v}$ provide the statistical measure of the velocity patterns of the turbulent atmosphere:

- $\overline{\Delta v}$ is the same dispersion velocity as the one defined in Eq. (5). The speckle boiling time is inversely proportional to this value.
- $\overline{v}$ is the averaged velocity of the turbulent layers:

$$\overline{v} = \frac{\int_0^{H} v(h)\, C_n^2(h) dh}{\int_0^{H} C_n^2(h) dh} \quad (12)$$

  The parameter $\overline{v}$, together with $\overline{\Delta v}$ determine boundaries for v^* (Appendix A) which is directly related to the optimum response time for adaptive optics and for Michelson interferometry as a whole.
- θ is the angle made between the subpupil direction and the mean direction of displacement of the turbulent layers. It is, in the Taylor sense, the main direction of motion of the wavefront corrugations. This parameter may be used in relation with recent work (Jorgenson et al. 1991) using the chaotic behavior of the turbulence to predict the wavefront evolution, thus increasing the efficiency of active correction systems.

Table 2. The parameters of the covariance, $A(D, d, \gamma)$, $B(D, d, \gamma)$ and $C(D, d, \gamma)$: a set of numerical solutions of the integral functions expressed in Appendix B for pupil diameters of 12 cm, 20 cm apart.

γ°	A(D, d, γ)	B(D, d, γ)	C(D, d, γ)
0	-0.150	-0.119	0
30	-0.199	-0.046	-0.152
60	-0.033	0.046	-0.196
90	-0.316	-0.119	0
120	-0.033	0.046	0.196
150	-0.199	-0.046	0.152
180	-0.150	-0.119	0

In the Eq. (12), $f(\overline{v},\theta,\overline{\Delta v},D,d,\gamma)$ is the covariance factor for the tilt velocity in front of the two subapertures. It may be computed as follows:

$$f(\overline{v},\theta,\overline{\Delta v},D,d,\gamma) = \left(\frac{\overline{v}^2\cos^2(\theta-\gamma) + \frac{1}{2}\overline{\Delta v}^2}{\overline{v}^2(1+2\cos^2(\theta-\gamma)) + 2\overline{\Delta v}^2}\right) A(D,d,\gamma) + \left(\frac{\overline{v}^2\sin^2(\theta-\gamma) + \frac{1}{2}\overline{\Delta v}^2}{\overline{v}^2(1+2\cos^2(\theta-\gamma)) + 2\overline{\Delta v}^2}\right) B(D,d,\gamma) + \left(2\frac{\overline{v}^2\sin(\theta-\gamma)\cos(\theta-\gamma)}{\overline{v}^2(1+2\cos^2(\theta-\gamma)) + 2\overline{\Delta v}^2}\right) C(D,d,\gamma) \quad (13)$$

$A(D, d, \gamma)$, $B(D, d, \gamma)$ and $C(D, d, \gamma)$ are integral functions expressed in Appendix B. As they do not possess analytical solutions they have to be computed numerically. Table 2 gives a set of solutions for pupils of 12 cm diameter separated by 20 cm.

The assumption of the kinematic model presented in Fig. 1 are multiple and thin moving atmospheric layers with inner frozen turbulence, near field approximation, and Kolmogorov inertial law for the turbulence spectrum.

Because a physical interpretation concerning the theory of the measurement is easier when neglecting the covariance term in the structure function equation, the first results presented in Sect. 5 are computed using this simplification. An error is generated on the estimate of the measured layers velocities and of the θ direction, respectively of about 4% and plus or minus 15 degrees.

4.2. New instrumental set-up

The share of the high frequency image wander is significant in the structure function $D_{\frac{\partial\alpha}{\partial t},\gamma}$. Because the classical seeing monitor detector controller has a too low sampling rate for our purpose (the minimum time between two read-outs of 20x20 pixels subimages is limited to 64 ms), an optical adaptor has been designed to increase the effective image acquisition rate.

A scanning device constituted by a tilt mirror mounted on a galvanometer is installed in the afocal beam after the roof prism of the seeing monitor, between the two usual lenses: collimator and CCD objective. When observing with the new set-up, the tilting mirror driven by a staircase signal shown in Fig. 3 moves the dual star image across the CCD detector after each exposure in a direction perpendicular to the subpupil separation (Fig. 2). Several dual images are therefore formed in the image plane detector, their temporal separation is directed by the step period. Their exposure time is determined by the aspect ratio of a chopping wheel occulting the light when the scanning mirror moves from one step to the other. The chopper also permits to avoid blurring of the individual stellar images caused by the finite impulse response time of the scanner (typically 0.4 milliseconds for small rotation angles). The shutter mentioned in Sect. 3.2 is triggered by the scanning signal with an exposure time adjusted to the transit time of the beams across the CCD.

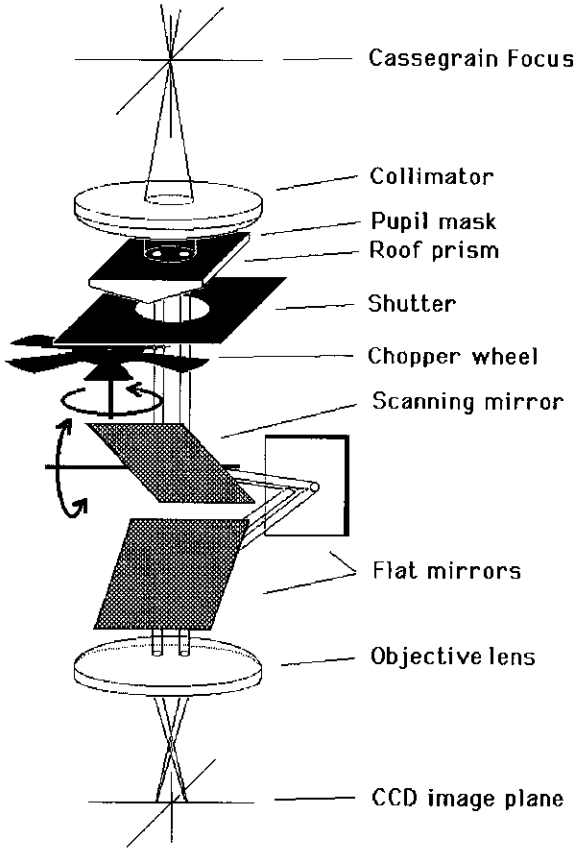

Fig. 2. Optical adaptor for the DIMM: a tilt mirror drives the dual star images across the CCD detector

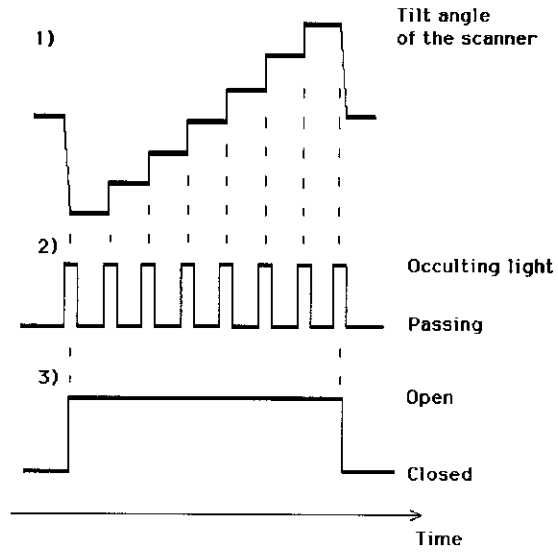

1) Staircase signal of the scanning mirror tilt angle, 2) Chopper wheel, 3) Shutter.

Fig. 3. Input signals used to obtain CCD frames containing several pairs of stellar images with submillisecond exposure time ($\sim$ 0.7 ms) separated by 2 ms

As a result, by means of this optical oscilloscope, two dimensional frames are obtained containing several pairs of stellar images with submillisecond exposure time ($\sim$ 0.7 ms) and a sampling rate of up to 500 Hz. The frame processing is done on line, it includes the detection of the stellar images and the determination of the position of their individual centroid. The differential image motion velocity is derived from the difference of the relative displacements of two adjacent pairs divided by their temporal separation.

4.3. Instrumental limitations

The pupil sizes are necessarily different from those used in classical DIMM operation. Because the exposure time per dual images is much shorter, photometric considerations impose an increase of the aperture diameter. Secondly, the choice of the pupil size determines the maximum wavefront velocity that can be measured without time-filtering effect. The time spectrum of the angle of arrival velocity has been previously analyzed (Lopez 1992). The condition for sampling the full bandwidth at Shannon frequency depends on the atmospheric conditions:

$$\sup(\frac{\nu r_0}{2}, \frac{\nu D}{2}) > \sup(\overline{v}, \overline{\Delta v}) \tag{14}$$

where D is the pupil diameter, ν the sampling rate of the system. For the 12 cm pupil diameter which are in use when observing temporal-coherence with the modified seeing monitor and for a sampling frequency of 500 Hz delivered by the adaptor, the maximum horizontal wavefront velocity properly measured is about 30 m/s.

The remaining uncertainty is caused by the error on the determination of the centroid position which generates a noise of variance $N^2_{\frac{\partial\alpha}{\partial t}}$ on the derived image velocity variance. $N_{\frac{\partial\alpha}{\partial t}}$ depends slightly on the direction γ, however its mean value can be estimated from the noise N^2_α on the position measurements given in Eq. (10) by:

$$\begin{aligned} N^2_{\frac{\partial\alpha}{\partial t}} &\approx 2\,\nu^2 N^2_\alpha \\ &\approx 10^{-7}\ \mathrm{rd}^2.\mathrm{s}^{-2} \text{ for } \nu = 500\,\mathrm{Hz}. \end{aligned} \tag{15}$$

Measurements of this quantity realized with an artificial source located at the Cassegrain focus lead to the following more realistic value including the effect of the tilt mirror and chopper wheel. The noise term averaged over all directions of measurement and for $\nu = 500$ Hz is given as a mean variance $\pm$ the rms of fluctuations around the mean:

$$N^2_{\frac{\partial\alpha}{\partial t}} = (1.25 \pm 0.03)\,10^{-7}\ \mathrm{rd}^2.\mathrm{s}^{-2}. \tag{16}$$

The noise term is statistically independent of the tilt velocity and can be subtracted out from the variance in every direction of measurement independently. $N^2_{\gamma,\frac{\partial\alpha}{\partial t}}$ is the sum of a systematic error and of a random quantity $\delta N^2_{\frac{\partial\alpha}{\partial t}}$ independent of the direction γ. After subtraction of the systematic error, $\delta N_{\frac{\partial\alpha}{\partial t}}$ sets

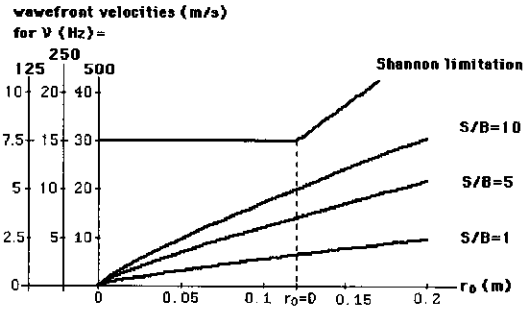

Fig. 4. Analysis of the trade-off between Signal to Noise ratio and Shannon limitation for different conditions of spatio-temporal coherence according to Eq. (14) with 12 cm diameter pupils

the signal to noise ratio on the computed velocity variance in the direction γ:

$$(\frac{S}{N})_\gamma = \sqrt{\frac{D_{\gamma,\frac{\partial\alpha}{\partial t}}}{\delta N^2_{\frac{\partial\alpha}{\partial t}}}} \tag{17}$$

and thus depends on r_0, $\overline{\Delta v}$, $\overline{v}$, θ, D, d and γ. We take the particular case of the longitudinal structure function with $\theta = \pi/4$. The structure function can be roughly simplified to:

$$D_{\frac{\partial\alpha}{\delta t}} = 0.512\,\lambda^2\, r_0^{-5/3}\, D^{-7/3}(\overline{v}^2 + \overline{\Delta v}^2) \tag{18}$$

Signal to noise ratio and Shannon limitation relations, both depending on r_0, $\overline{\Delta v}$, $\overline{v}$, are plotted together in Fig. 4. This diagram allows to determine the sampling frequency at which $\overline{\Delta v}$, $\overline{v}$, versus r_0 are correctly measured: decreasing the image motion acquisition frequency improves the signal to noise ratio but, on the other hand the Shannon theorem limits the maximum velocity properly measured. Therefore the acquisition frequency must be adapted in real time to the turbulent conditions. The sampling rate of the coherence monitor is changed accordingly by recomputing the variance on the same time series with a time lag increasing from one to four samples. This method simulates a frequency variation from 500 Hz to 125 Hz, among which the result with the highest signal to noise ratio verifying Eq. 14 is chosen.

5. First results of measurements made at La Silla

The modified differential image motion monitor is installed on a tower 5 meters above ground at the La Silla Observatory close to the Schmidt telescope. The data presented hereafter correspond to 7 nights of continuous monitoring realized in coordination with the first technical run of the Come-On-Plus adaptive optics system installed on the 3.6 m telescope in December 1992 (Hubin et al. 1992). The first statistical measures on turbulent layers allowing the wavefront time characteristics to be determined were in fact obtained with the same instrument at Paranal during the PARSCA Campaign in March 92 (Sarazin 1992), but with a degraded accuracy. The spatio-temporal parameters of the atmosphere, namely seeing, scintillation, average and dispersion velocities, and average direction were monitored each

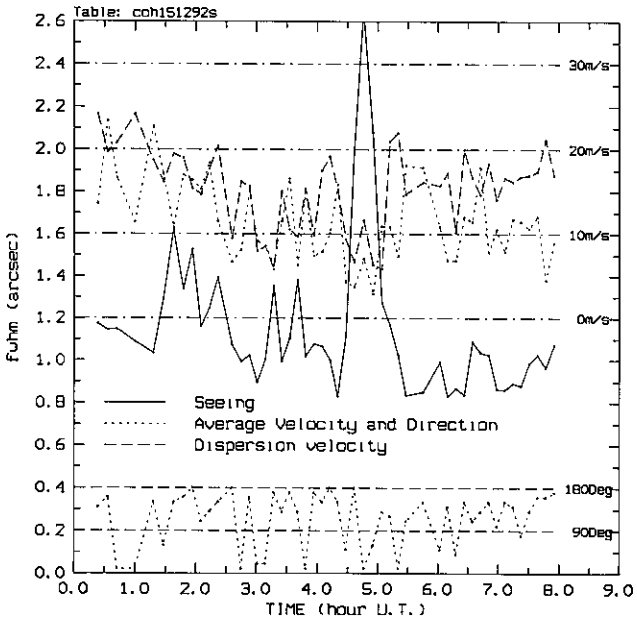

Fig. 5. A complete night of measurements of the kinematic parameters of the turbulent atmosphere on December 15, 1992 at La Silla. The average direction of the tilt has a 180 degree symmetry

night at a rate of one estimate every 8 mn on the basis of 200 image pairs. The output rate of the coherence monitor is currently limited by the computing power installed and should be closer to 2 mn for a correct sampling of atmospheric changes. Figure 5 shows a complete night of measurement of the kinematic parameters of the turbulent atmosphere, illustrating the partial decorrelation between the velocity of the wavefront and its spatial coherence. Figure 6 presents histograms displaying the data on r_0, $\overline{\Delta v}$, $\overline{v}$ and on the speckle life time.

Acknowledgements. This work was supported by ESO as a part of the VLT Astronomical Weather Station (AWS) instrumentation package, following a suggestion by J. Beckers. The first possible observations were obtained thanks to the continuous technical help of R. Castillo, M. Morhinweg and G. Timmermann from La Silla TRS department, of J. Navarrete from VLT Site and Building Services at Paranal, and of the DIMM operators at Cerro Paranal.

Thanks also to technical help of Y. Bresson and P. Antonelli from OCA Observatory. We wish also thank J. Gay, P. Léna, D. Mékarnia, Ch. Perrier and F. Roddier for helpful comments and encouraging discussions. Thanks also J. Colin for his help in the preparation of the paper

Appendix A

The mean velocity of wind for turbulent layers, useful to express the optimum exposure time for Michelson Interferometry is given by

$$v^* = \left[\frac{\int_0^\infty |\, v(h)\,|^{5/3}\, C_n^2(h)dh}{\int_0^\infty C_n^2(h)dh}\right]^{3/5}$$

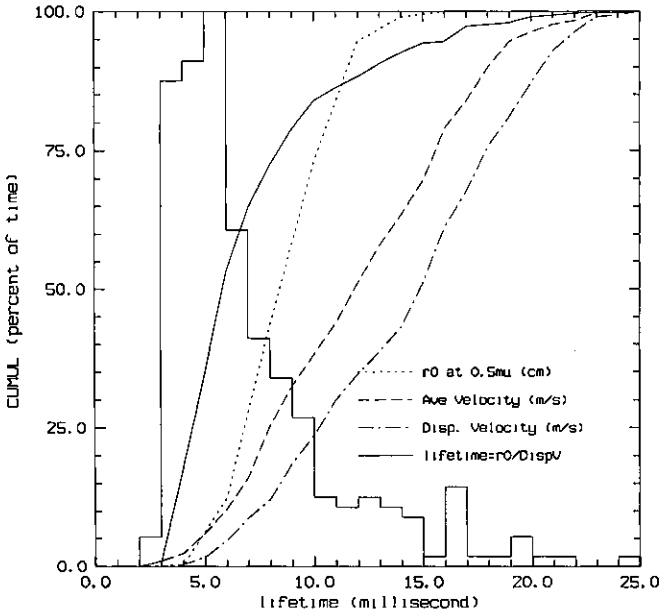

Fig. 6. Histograms of τ and probability distribution corresponding to 1 week of data on r_0, $\overline{\Delta v}$, $\overline{v}$ and on the speckle life time as defined in Eq. (4)

which ranges between

$$\frac{\int_0^\infty v(h)\, C_n^2(h)dh}{\int_0^\infty C_n^2(h)dh} \leq v^* \leq \left[\frac{\int_0^\infty |\, v(h)\,|^2\, C_n^2(h)dh}{\int_0^\infty C_n^2(h)dh}\right]^{1/2}$$

According to the presented method that allows the measures of $\overline{\Delta v}$ and $\overline{v}$ the inequality is

$$\overline{v} \leq v^* \leq [\overline{v}^2 + \overline{\Delta v}^2]^{1/2}$$

Appendix B

$$A(D,\, d,\, \gamma) = 1.431\, D^{1/3} \iint_{-\infty}^{+\infty} f_x^4\, f^{-17/3}\, J_1^2(\pi D f)$$
$$\cos(2\pi\, \mu(f_x \cos\gamma + f_y\, \sin\gamma))df_x\, df_y$$

$$B(D,\, d,\, \gamma) = 1.431\, D^{1/3} \iint_{-\infty}^{+\infty} f_x^2 f_y^2 f^{-17/3}\, J_1^2(\pi D f)$$
$$\cos(2\pi\mu(f_x \cos\gamma + f_y\, \sin\gamma))df_x df_y$$

$$C(D,\, d,\, \gamma) = 1.431\, D^{1/3} \iint_{-\infty}^{+\infty} f_x^3 f_y f^{-17/3}\, J_1^2(\pi D f)$$
$$\cos(2\pi\mu(f_x \cos\gamma + f_y\, \sin\gamma))df_x df_y$$

with $f = (f_x^2 + f_y^2)^{1/2}$

where f_x and f_y are spatial frequencies, μ is the subpupil separation, J_1 is the first order Bessel function.

References

Abitbol, M., Subovitch, N., Ben-Yosef, N., 1991, I.C.O. Top. Meeting on Atmospheric, Volume and Surface Scattering and Propagation, Florence, Italy.

Aime, C., Borgnino, J., Martin, F., Petrov, R., Ricort, G., Kadiri, S., 1986, J.O.S.A. A, 3, 1001.

Colavita, M.M., Shao, M., Staelin, D.H., 1987, Applied Optics, 26, 4106.

Fried, D.L., 1975, Radio Science, 10, 71.

Hubin, N., Beuzit, J.L., Gigan, P., Léna, P., Madec, P.Y., Rousset, G., Boyer, C., Gaffard, J.P., Richard, J.C., Vittot, M., Rigaut, F., Gendron, E., Merkle, F., 1992, ESO preprint No. 48, S.P.I.E. 1780.

Jorgenson, M.B., Aitken, G.J.M., Hege, E.K., 1991, Optics Letters, 16, 2.

Lopez, B., Sarazin, M, 1991, Proc. ESO-Conf. on High Resolution Imaging by Interferometry II; Garching.

Lopez, B., 1992, A&A, 253, 635.

Müller, M., Baier, G., Helm, S., Weigelt, G., 1988, Proc. NOAO-ESO conf. on: High-resolution imaging by Interferometry, Garching.

Roddier, F., 1981, Progress in Optics, 19, 281.

Roddier, F., Gilli, J.M., Lund, G., 1982, J. Optics, 13, 5.

Roddier, F., Léna, P., 1984, J. Optics, 15, 171.

Sarazin, M., Roddier, F., 1990, A&A, 227, 294.

Sarazin, M., 1992, The Messenger, No. 68.

Scaddan, R.J., Walker, J.G., 1978, Applied Optics, 17, 23.

Soules, D.B., Drexler, J.J., Waldie, A.H., Qualtrough, J.A., Eaton, F.D., Peterson, W.A., Hines, J.R., 1989, Tech. Sympos. on Aerospace Sensing, S.P.I.E. 1115.

Vernin, J., Weigelt, G., Caccia, J.L., Müller, M., 1991, A&A, 243, 553.

This article was processed by the author using Springer-Verlag LaTeX A&A style file version 3.

Astron. Astrophys. 276, 327–330 (1993)

ASTRONOMY
AND
ASTROPHYSICS

Abstracts of articles which have been published in A. & A. Supplement Series, Vol. 100, No. 2

Photometric distances to the nearby galaxies IC 10, IC 342, and UGCA 86, visible through the Milky Way

I.D. Karachentsev and N.A. Tikhonov

Photographic B, V photometry of the bright stellar population has been made for three nearby galaxies which lie at a low galactic latitude. Relying on the brightest red and blue supergiants we obtained the following distances: 1.0 Mpc for IC 10, 2.1 Mpc for IC 342, and 1.9 Mpc for UGCA 86.

1993, A&AS 100, 227-235

Electron-impact widths of four- and five-times charged ion lines of astrophysical importance

M.S. Dimitrijević

Stark widths of astrophysically important spectral lines within 3 C V, 50 O V, 12 F V, 9 Ne V, 3 Al V, 6 Si V, 11 N VI, 28 F VI, 8 Ne VI, 7 Na VI, 15 Si VI, 6 P VI, and 1 Cl VI multiplets, have been calculated by using a modified semi-empirical approach.

1993, A&AS 100, 237-241

Study of proper motions in the region of the open cluster M67 and membership of stars

J.L. Zhao, K.P. Tian, R.S. Pan, Y.P. He and H.M. Shi

Relative proper motions and membership probabilities of 1046 stars in the open cluster M67 area are determined from PDS measurements of 9 plate pairs taken with the double astrograph at the Zô–Sè station of Shanghai Observatory, which has an aperture of 40 cm, a focal length of 6.9 m and a scale of 30″/mm. The number of stars with membership probabilities higher than 0.8 and at a distance less than 45′ from the field center is 282. The average standard errors of proper motions vary from ± 0.″0004/yr for bright stars in the inner part of the field to some ± 0.″0015/yr for faint stars in the outer part of the cluster. It is shown by a detailed discussion that the proper motions and membership probabilities of the stars determined in this paper are in quite satisfactory agreement with those obtained by Sanders (1977) or Girard et al. (1989).

1993, A&AS 100, 243-261

Optical positions and 327 MHz flux-densities of UGC galaxies in selected Westerbork fields

C. Oly and F.P. Israel

We present accurate optical positions of 421 UGC galaxies which we used to search thirty 92 cm (326 MHz) WSRT fields observed for other purposes for emission from these galaxies. Good 92 cm flux-densities were obtained for 140 galaxies, marginal flux-densities for 71 galaxies and upper limits for 210 galaxies. Thus, we detected half of all UGC galaxies in the observed fields. For 35 galaxies we have determined spectral indices in the decimeter wavelength range. The mean

spectral index for spiral galaxies ($\alpha = 0.72 \pm 0.03$) is very similar to that of elliptical galaxies ($\alpha = 0.64 \pm 0.10$). The four multiple systems in the sample have a much flatter spectral index ($\alpha = -0.21 \pm 0.07$) which suggests the presence of a significant thermal component in their total radio emission. The monochromatic radio luminosity of the detected galaxies is sharply peaked between $L_{92} = 10^{22}$ and 10^{23} W Hz^{-1}. Comparison with IRAS results show that about half of the galaxies detected at radio wavelengths are detected in the far-infrared (i.e. a quarter of all galaxies). Virtually no E/SO galaxies were seen. The correlation of 100 micron emission with optical brightness is significantly better than the correlation of radio with optical brightness for the spiral galaxies in the sample. Both relations are approximately linear. Almost all galaxies brighter than $m_p = 14.0$ mag were detected both in the radio and the infrared. The data suggest that some spiral galaxies are anomalously weak in the infrared as compared with their radio brightness, but this needs confirmation.

1993, A&AS 100, 263-285

The W 80 dark cloud: a case study of fragmentation. I. The observations

C. Feldt and H.J. Wendker

We present maps of the W 80 dark cloud ($2° \times 2°$) from fully sampled surveys in ^{12}CO, ^{13}CO, H_2CO and HI. The observations are described in detail. Due to the choice of the above species a volume density range between 10 and 10^5 cm^{-3} is probed. The expectation that this dark cloud is relatively quiescent and young with regard to ongoing fragmentation is confirmed. The data will be used for a study of the inventory of structure and its fragmentation status.

1993, A&AS 100, 287-303

Measures of close binaries observed at the Pic du Midi Observatory (*Text in French*)

P. Couteau, J.A. Docobo et J. Ling

Table 1 gives 241 measures of 119 close binaries observed with 2 m Telescope Bernard Lyot at Pic du Midi Observatory. Measurements were made by micrometer with illuminated wires.

1993, A&AS 100, 305-310

Analysis of IRAS stellar sources in α Persei region

E. Trullols and C. Jordi

The present study is an analysis of infrared sources in the α Persei open cluster region from the IRAS *Point Source Catalog* and from ground based photometric observations. Cross-identification between stars in the region and IRAS *Point Source Catalog* was performed and 9 new associations were found. *BVRI* Johnson photometry for 24 of the matched objects have been carried out. Physical identity of visual and IRAS sources, and relationship to the α Persei open cluster are discussed.

1993, A&AS 100, 311-318

The light variations of some southern CP2 stars

F.A. Catalano and F. Leone

Nine southern chemically peculiar stars brighter than the seventh visual magnitude have been observed in the *uvby* system. All the stars but HD 148199 are previously known light variables, although their periods were not accurate enough to phase together different kinds of observations carried out several years apart. Here we present more refined values of the period for the stars: HD 74521, HD 90044, HD 119419, HD 125630, HD 137509, HD 147010, HD 166469 and HD 170397. The star HD 148199, formerly considered constant in light, has been found to be variable in light too with the same period as the magnetic field.

1993, A&AS 100, 319-330

BV photometry and Hα spectroscopy of the RS Canum Venaticorum binary V711 Tauri

S. Mohin and A.V. Raveendran

Differential BV photometry of V711 Tau obtained on a total of 120 nights during the years 1984-91 and Hα spectroscopy obtained on 14 nights during the 1990-91 observing season are presented. We find that the mean light level of the system the period 1975-82 was fainter by ~ 0.05 mag than that during the period 1982-91. The change in the mean light level during probably arises from a global reduction in the area of spots or from the disappearance of spots from the polar region. At larger amplitudes the brightness at minimum decreases and the brightness at maximum increases, both converging to a particular value of ΔV at very low amplitudes. Phase of light minima observed during 1975-91 lie on two independent near-straight lines, implying that spots are confined predominantly to two different latitude belts. The Hα equivalent widths did not show any orbital modulation during the period of our observations. The spectra obtained on one night (1991 Feb. 6) show a sudden drop in equivalent width; this occurs during the descending branch of the light curve.

1993, A&AS 100, 331-342

The importance of surface inhomogeneities for K and M dwarf chromospheric fluxes

P.M. Panagi and M. Mathioudakis

We present published and archived spectroscopic and spectrophotometric data of H_α, Ca II, Mg II and X-ray for a large sample of K and M dwarfs. The dataset points to the importance that surface inhomogeneities have in the flux luminosity diagrams in these late-type dwarfs, irrespective of whether the Balmer lines are in emission or absorption. Although supporting the fact that cooler stars exhibit increasing levels of surface activity, evident through an increasing incidence of Balmer emission, surface inhomogeneities, or variations in the local temperature and density structure, at the chromospheric level, dominate the total Ca II and Mg II fluxes. We show that the flux-flux and luminosity-luminosity relations indicate differing extents of inhomogeneity from the chromosphere through to the corona. A good correlation between Ca II and Mg II fluxes indicates that they are formed in overlapping regions of the chromosphere, so that contribution of surface inhomogeneities is not evident from this particular flux-flux diagram. In the region of the upper chromosphere through to the transition and corona, the correlation between Ly_α and X-ray fluxes indicates regions with similar levels of areal inhomogeneity. This appears to be uncorrelated with that at the chromospheric level. From a direct comparison of the Ca II and H_α observations with the computed models of Cram & Giampapa, it appears that the mean chromospheric temperature decreases with increasing effective temperature, implying either more energy available.

1993, A&AS 100, 343-369

A decade of photometric observations of young stars - with special comments on periodicities

G.F. Gahm, E. Gullbring, C. Fischerström, K.P. Lindroos and K. Lodén

We have collected photometric observations of 16 young stellar objects during 10 observing periods from 1981 to 1991. The photometry includes measurements with broad-band Strömgren *uvby* and standard *UBVRIJHKL* intermediate filters in addition to narrow-band Hα and Hβ filters. A large part of the material has been discussed elsewhere and the purpose of the present article is to publish all individual measurements, to comment on light curves and colour diagrams not presented before and to make a search for periodic light fluctuations. The material includes 8 classical T Tauri stars (CTTS), 5 weak-line T Tauri stars (WTTS), 2 post T Tauri candidates (PTTS) and 1 Herbig Ae star. We have searched for periodic light variations in 15 of the stars, of which 7 have not been followed photometrically before. None of the CTTS shows distinct periods. On this basis and a literature survey published elsewhere we conclude that many announced periods are still doubtful. Many of these stars tend to brighten and fade on certain time-scales which can differ from time to time. We also arrive at the conclusion that nevertheless about 1/4 of the CTTS studied so far have well defined periods. All five WTTS show evidence of regular fluctuations of small amplitudes on time-scales of a few days but for 3 stars (San 1, Andrew 481, SZ Cha) the data base is too small for any definite conclusions to be drawn. The amplitudes of the variations increase with decreasing wavelength and rotational modulation of dark spots on the stellar surface is consistent with such variations. In this picture Sz 82 (Thé 12), with a period of 1.2 days, is a fast rotator with pronounced ultraviolet activity and X-ray emission. RY Lup is a well studied case with an established period of 3.75 days. It is a special case of WTTS since it carries

a large infrared excess. One PTTS was followed over several nights but shows no evidence of periodicity. For the Herbig Ae star AB Aur no period can be announced at present even though one Fourier method based on CLEAN does indicate periods close to what has been found from spectral line variability.

1993, A&AS 100, 371-393

Spectroscopic observations of radio source identifications from the 1 Jy, S4 and S5 surveys. III.

M. Stickel and H. Kühr

Optical spectra are presented for the optical counterparts of 21 radio sources taken from the 1 Jy, S4, and S5 radio source catalogues. New redshifts are given for 18 sources, including a radio-selected quasar with a redshift of $z = 3.886$. For two other sources, redshifts had previously been listed in other publications and were confirmed by the new observations. Finally, one radio source is confirmed as a BL Lac object showing a featureless spectrum. For several sources, additional direct imaging data are provided.

1993, A&AS 100, 395-411

A systematic study of IRAS selected proto-planetary nebula candidates. I. Selection of the sample and observations of the southern objects

J.Y. Hu, S. Slijkhuis, T. de Jong and B.W. Jiang

This paper is the first of a series, in which we report an extensive study of a sample of 62 IRAS selected proto-planetary nebula candidates. In this paper we describe the selection of the sample. For the 42 southern sources in the sample we present the results of observations using optical and near-infrared photometry, and optical spectroscopy. Out of the 42 sources, 26 are associated with an optical counterpart, 12 do not have an optical counterpart, and 4 sources have more than one possible optical counterpart. Spectroscopy is carried out for 18 sources. Spectral types are mainly M, G and F. The photometric observations show that nearly all sources in the sample radiate the bulk of their energy in the IRAS infrared. This implies that the sources are surrounded by a thick dust shell.

1993, A&AS 100, 413-430

Analysis of the distribution of HII regions in external galaxies. II. Analysis of the spiral structure

C. García Gómez and E. Athanassoula

This paper is the second of a series where we study the distribution of HII regions in spiral galaxies. We use a Fourier decomposition to obtain the main spiral components of 44 galaxies, extracted from the sample of García Gómez & Athanassoula (1991) as those having some structure in their HII region distribution. We recompose the density distribution using more than one component from each Fourier spectrum, thus obtaining more accurate results than in previous studies. We also study the dependences of the pitch angles of these components on other physical parameters of the galaxies, like the Hubble type and the arm class. Finally, for the galaxies where information on the flux of the HII regions is available, we use the Fourier decomposition to separate the HII regions in the arms from those in the interarm zones. The HII regions in the arms are, on the average, brighter by a factor of the order of 1.25 than those in the interarm. The brightest HII regions are preferentially located in the arms.

1993, A&AS 100, 431-464
